Progress in Neurobiology 231 (2023) 102541

Contents lists available at ScienceDirect

Progress in Neurobiology

journal homepage: www.elsevier.com/locate/pneurobio

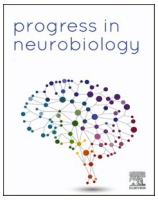

STED microscopy reveals dendrite-specificity of spines in turtle cortex

Jan A. Knobloch [a], Gilles Laurent [b], Marcel A. Lauterbach [a,b,*]

[a] Department of Molecular Imaging, Center for Integrative Physiology and Molecular Medicine, Saarland University, Building 48, 66421 Homburg, Germany
[b] Max Planck Institute for Brain Research, Max-von-Laue-Str. 4, 60438 Frankfurt am Main, Germany

ARTICLE INFO

Keywords:
Dendritic spine
Dendrite-specific
Turtle cortex
STED microscopy
Spine morphology

ABSTRACT

Dendritic spines are key structures for neural communication, learning and memory. Spine size and shape probably reflect synaptic strength and learning. Imaging with superresolution STED microscopy the detailed shape of the majority of the spines of individual neurons in turtle cortex (*Trachemys scripta elegans*) revealed several distinguishable shape classes. Dendritic spines of a given class were not distributed randomly, but rather decorated significantly more often some dendrites than others. The individuality of dendrites was corroborated by significant inter-dendrite differences in other parameters such as spine density and length. In addition, many spines were branched or possessed spinules. These findings may have implications for the role of individual dendrites in this cortex.

1. Introduction

Dendritic spines are the targets of most excitatory synapses onto spiny excitatory neurons in the vertebrate brain (DeFelipe and Fariñas, 1992). They are considered key structures (Yuste, 2010; Tønnesen and Nägerl, 2016) whose shape likely impacts synaptic strength and efficacy (Araya et al., 2014). The spine neck is important for the electrical, diffusional and biochemical isolation of the synapse from its parent dendrite (Harris and Stevens, 1988; Harris and Stevens, 1989; Yuste and Denk, 1995; Yuste et al., 2000; Nusser et al., 2001) and postsynaptic currents are positively correlated with spine size (Matsuzaki et al., 2004). In addition, dynamic structural changes of dendritic spines have been implicated in cognition and memory (Kasai et al., 2010; Runge et al., 2020; Dunaevsky et al., 1999).

Differences of spine number or density may therefore translate into functional differences in a local circuit (Benavides-Piccione et al., 2013). Such differences have indeed been reported in mice (Ballesteros-Yáñez et al., 2006) and primates, with more than 3-fold variations in spine density across brain areas (Jacobs, 2001; Elston et al., 2001).

To better understand the potential importance of spine shape, detailed morphological data are needed, but still scarce. Spines are commonly classified into few categories ("thin", "mushroom", "stubby" and "filopodia") (Peters and Kaiserman-Abramof, 1970; Benavides--Piccione et al., 2013), although these categories clearly depend on imaging resolution (Tønnesen and Nägerl, 2016; Tønnesen et al., 2014) and thus probably represent the coarse binning of a continuum (Pchitskaya and Bezprozvanny, 2020).

The correlations observed between functional and morphological characteristics of spines (Araya et al., 2014; Padmanabhan et al., 2021; Arellano et al., 2007) suggest that morphological features alone might be used as a proxy for functional information. For example, a complete map of input strengths inferred from dendritic morphology could help us predict or interpret neuronal computation (Arellano et al., 2007).

Serial-section electron microscopy is the gold standard for detailed morphological reconstruction of single spines in three dimensions, (Harris and Stevens, 1988; Denk and Horstmann, 2004). However, with this technique, spines are often reconstructed only in limited parts of cells and dendrites [although see (Svara et al., 2022, Boergens et al., 2018)]. By contrast, light microscopy allows one to image large fields of view, but the resolution of conventional light microscopy is insufficient to visualize the details of spine morphology.

A recent study combining expansion microscopy with lattice light-sheet microscopy carried out high-resolution imaging of mouse brains on a large scale (Gao et al., 2019). This study found layer-specific spine characteristics. Other studies, based on confocal/widefield images with limited spatial resolution, report the existence of differences between spines on basal and apical dendrites in human pyramidal cells (Benavides-Piccione et al., 2013; Luengo-Sanchez et al., 2018). We are not

Abbreviations: STED, Stimulated emission depletion; DVR, Dorso-ventricular ridge.

* Corresponding author at: Department of Molecular Imaging, Center for Integrative Physiology and Molecular Medicine, Saarland University, Building 48, 66421 Homburg, Germany.
E-mail address: Marcel.Lauterbach@uni-saarland.de (M.A. Lauterbach).

https://doi.org/10.1016/j.pneurobio.2023.102541
Received 9 June 2023; Received in revised form 20 October 2023; Accepted 21 October 2023
Available online 26 October 2023

aware that such differences have been described in mice (Konur et al., 2003).

Very little is known about spines in other model organisms, such as reptiles, although spiny neurons have long been described there. Using Golgi stains, long spines have been found in medium spiny neurons in the dorsolateral striatum of the turtle *Trachemys scripta elegans* (González et al., 2013). Ebner et al. distinguished two spine types in electron micrographs of *Trachemys scripta* (Ebner and Colonnier, 1975). Basic dendrite and spine characteristics have been compared, using small subsets of spines in electron and light microscopy in four different turtle species (Goncharova and Davydova, 1983).

This scarce knowledge about spines in turtles is surprising, given that the identification of general principles should benefit from the study of many well-chosen model systems (Hemberger et al., 2019; Laurent, 2020). The cortices of reptiles and mammals living today all originate from a shared ancient cortex, implying that they may retain features of this common ancestry in their function, connectivity, and structure (Hemberger et al., 2019). With only three layers, turtle cortex has an architecture similar to mammalian hippocampus or olfactory cortex; it is evolutionarily linked to the mammalian neocortex that has six layers (Riquelme et al., 2023). Dorsal cortex is the first cortical stage of visual processing, receiving retinal inputs via the thalamic lateral geniculate nucleus (Fournier et al., 2018). Because the cortex is floating on a large ventricle, cortex samples can be obtained that are handled similar to typical rodent slices, but where a non-cut surface is observed; also superficially positioned neurons are thus entirely intact.

Here, we capitalize on this preparation and on the super-resolution features of STED microscopy to study this ancient cortex. STED-microscopy (Hell and Wichmann, 1994; Hell, 2007; Lauterbach, 2012) provides not only time-resolved high-resolution images, e.g., of neuronal processes (Westphal et al., 2008; Lauterbach et al., 2016; Lauterbach et al., 2010; Steffens et al., 2021) but can also resolve subcellular neuronal structures with high contrast (Rangaraju et al., 2019; Willig et al., 2006). We examined spiny neurons in the turtle dorsal cerebral cortex and observed that the dendrites of single neurons differ from one another with regard to spine density and composition, suggesting mesoscopic organization of dendrites in this system.

2. Results

We imaged almost all the spines in three spiny neurons in the deep layer 2 of the turtle cortex (9308 spines in total) using high-resolution STED microscopy in paraformaldehyde-fixed tissue. Overview 3D-stacks acquired in confocal microscopy at low magnification (Fig. 1a–c) show that the neurons have a large spatial coverage with up to 850 µm span of the dendritic tree. Their dendrites are to a large extent in a plane parallel to the ventricular surface. They were subsequently imaged in 3D at high resolution with STED microscopy using a toroidal ("donut") depletion pattern for lateral resolution enhancement. We took advantage of the fact that cells were labelled in isolation in each preparation; the contrast was thus high (Methods) and the neurons were imaged only along the dendrites, reducing greatly the total volume imaged (1.8–12.2% of the cuboid enclosing each neuron). This also reduced bleaching, recording time and the amount of data to be stored and handled. The overall 3D morphology of each neuron was reconstructed by stitching the skeletonized STED images (Fig. 1d–f), giving an almost complete 3D outline

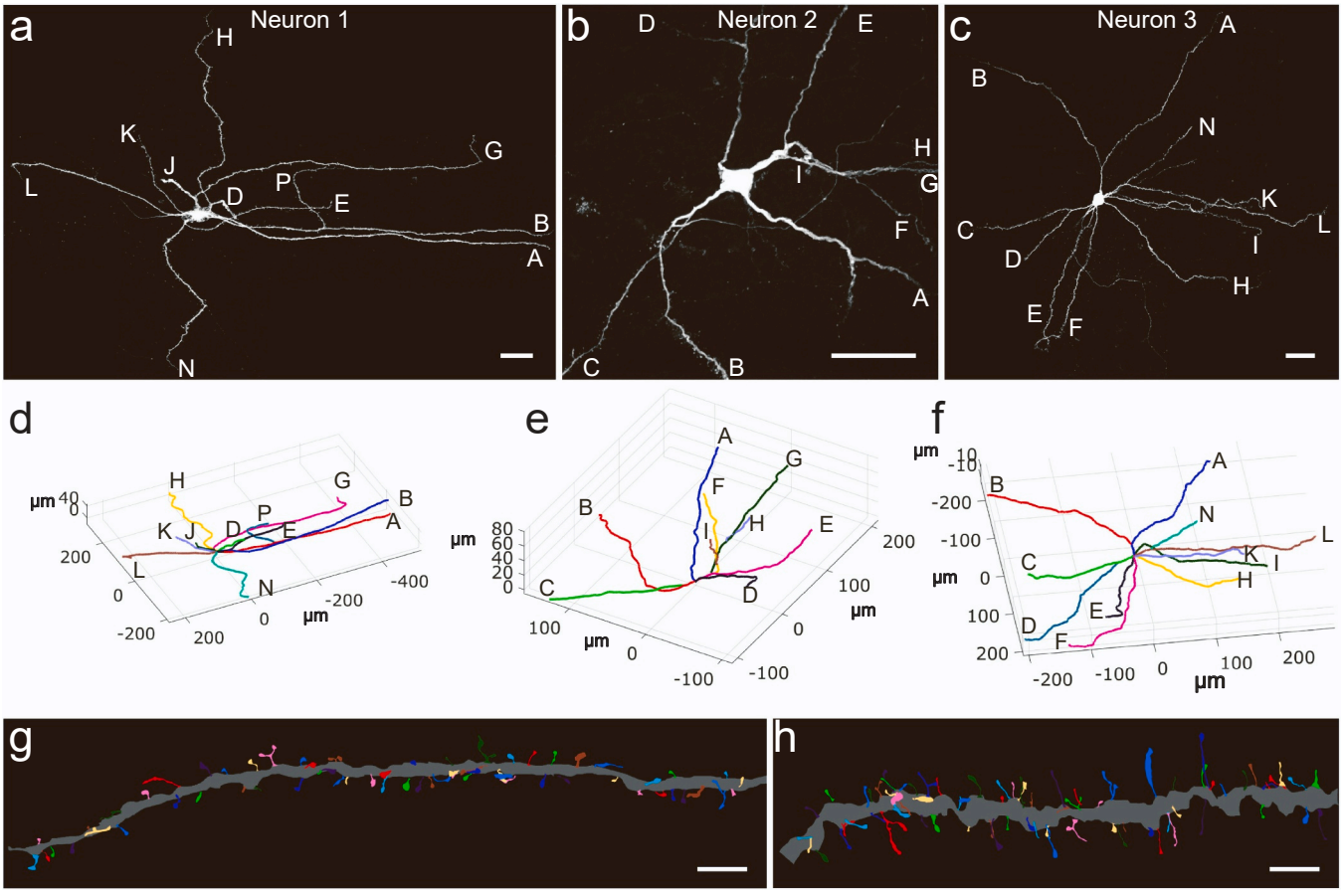

Fig. 1. Turtle neurons, (a–c) Confocal overviews of three cortical turtle neurons (maximum-intensity projections) show the large extent of the dendritic arbors; scale bars 50 µm. (d–f) Skeleton reconstruction based on individual high-resolution STED images along each dendrite. Dendrites in a–f are labeled with letters for later reference. (g–h) Segmentation of all spines shows that some dendrites have longer spines than others (zoom on dendrites B and H from the neuron 1 shown in a and d); scale bars 5 µm.

of the dendrites. This revealed the rather straight shape of most dendrites, with occasional sharps bends. STED microscopy gave a much more detailed view of the spines than two photon-microscopy, typically used to record and classify spines. The segmentation of 6943 spines (Fig. 1g, h) allowed us to describe their morphology in detail. We clustered spines according to their shapes in 3D and lengths. In addition and independently of the clustering, we described them with 10 morphological parameters (like length, head width, neck width, thickness variations, see Methods).

2.1. Multi-headed spines

At STED resolution (laterally 45 nm, axially 550 nm), we found a multitude of spine shapes, and among them multi-headed spines. Five hundred and four spines (i.e., 5.4% of all spines analyzed) had 2, 3, 4 or even 5 heads (Fig. 2a). The heads of these multi-headed spines could have similar (Fig. 2a (i)– (iv)) or very different sizes (Fig. 2a (v)–(xviii)). The multiple heads of a same spine could lie in close proximity of one another (Fig. 2a (xvii)–(xix)) such that they could possibly be enclosed inside a single presynaptic ending (Bastians, 2018); others were far from one another (Fig. 2a (xx)–(xxiv)). Various configurations could be observed for spines with three heads: some had a branching neck, such that each head has its own neck emerging from a common parent neck (Fig. 2a (xxv)–(xxvii)); others had heads budding from one long common neck (Fig. 2a (iv), (xxviii)–(xxx)). Occasionally a long spine laid parallel to the dendrite (Fig. 2a (xxxi)). Others yet seemed to surround unstained (and unidentified) structures (Fig. 2a (xxxii)–(xxxiv)).

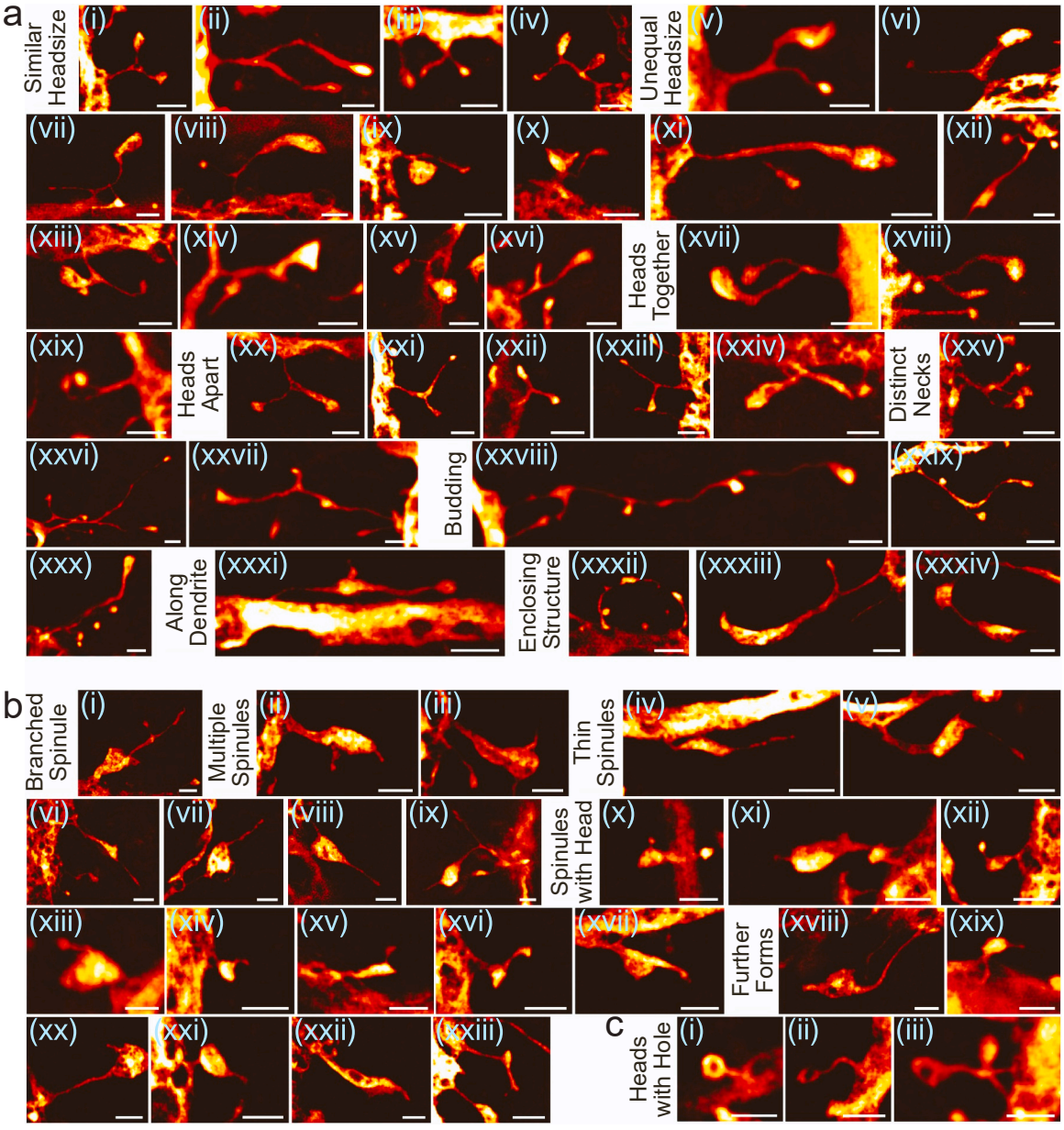

Fig. 2. Spines can have multiple heads and spinules, (a) Branched spines with multiple heads (5.4% of spines observed) can have several head of similar size (i)–(iv) or of very unequal size (v)–(xvi), present heads close together (xvii)–(xix) or far apart (xx)–(xxiv). They can have more than two heads with individual necks (xxv)–(xxvii) or rather budding from a common neck (xxviii)–(xxx); they can run parallel to the dendrite (xxxi). Some branched spines seem to enclose non-stained structures (xxxii)–(xxxiv). (b) Various forms of spinules are observed on 0.8% of spines. This includes branched spinules (i), multiple spinules on one spine head (ii)–(iii), thin, filopodia-like spinules (iv)–(ix), spinules with a mini-head (x)–(xvii) and further diverse forms (xviii)–(xxiii) (c) Some spines show pronounced "holes", presumably organelles or enclosed presynapses. Scale bars 1 μm.

2.2. Spinules

Seventy five (0.8%) among the spines analyzed had smaller structures, so called "spinules" (Westrum and Blackstad, 1962), budding off the spine head (Fig. 2b). The spinules could even themselves be branched (Fig. 2b (i)) and individual spines could have multiple spinules (Fig. 2b (ii), (iii)). Some were thin filopodium-like protrusions (Fig. 2b (iv)–(ix)); others consisted of a "mini-head" protruding from a "mini--neck" (Fig. 2b (x)–(xvii)). Further forms, often a short "finger" protruding from the head, were observed (Fig. 2b (xviii)–(xxiii)).

In some instances, apparent "holes" were observed in the spines (Fig. 2c), suggestive of inclusions in spines or of the engulfment of a presynaptic terminal (Bastians, 2018).

2.3. Clustering of conventional spines

To determine if regular spines (i.e., spines with one head) form distinguishable classes, we clustered them using hierarchical clustering based on their morphology (diameter profile) and length (Fig. 3a, top row). To determine the optimal number of classes, we used the Davies-Bouldin criterion (Davies and Bouldin, 1979) with which we identified five classes. The Davies Bouldin criterion determines the optimal number of clusters based on the ratio of within-cluster and between-cluster distances (see Methods for details). We named the classes according to spine shape and size: "Stocky", "Dwarf", "Club-like", "Balanced", "Delicate". Even the Stocky spines typically had a detectable neck (Fig. 3a), which is very short. Dwarf spines had a longer neck, often with an ellipsoid head. Club-like spines had gradually thickening heads almost from the point where they emerged from their parent dendrite in contrast to the other classes, which had distinct neck and head regions. Balanced spines are longer than Dwarf spines and have sometimes elongated heads. Delicate spines are the longest ones with a think, long neck. Spine length varied greatly between 0.67 μm on average for Stocky spines and 4.06 μm (6 times larger) for the Delicate ones. Spines with a large head typically had a wide neck (Fig. S1a–c) and were long (Fig. S1d–f).

To check for the stability of clustering, we clustered the spines from each neuron individually (without taking into account the other neurons). This led to classes that matched in general those from the global clustering (i.e. all neurons taken together): Up to 98% of the spines of a given class as determined on one neuron belonged to the according class determined on all neurons together. Only in three out of the 15 individual clusters (five clusters on each of three neurons) less than 50% of the spines were assigned to the corresponding global clusters (Fig. S2).

2.4. Differences in spine composition across dendrites

We next examined whether spines that belong to different clusters intermixed randomly along single dendrites: visual inspection hinted at the possibility of non-random distributions (Fig. 1g, h). Indeed, quantitative analysis revealed that spines of a given class were not equally likely to be found on each dendrite of a same neuron (Fig. 3b). Said differently, each dendrite had a unique signature, made of different ratios of each spine class. This is also visible by color-coding each spine by class along each dendrite (Fig. 3c–e). The distribution of the classes along the dendrite is not clearly inhomogeneous (Fig. S3). The distribution of all spines belonging to a certain class onto the different dendrites was consequently also inhomogeneous (Fig. 3f). The spine-class distributions across all dendrites of all three neurons were significantly different (Pearson's Chi Square test, $p < 10^{-100}$). Comparing ratios of spine classes on the dendrites of individual neurons, spine classes differed significantly on the dendrites of neurons 1 and 2 ($p < 10^{-22}$, $p < 10^{-14}$), but no significant differences were observed for neuron 3. Pairwise comparisons of all dendrites of each of neurons 1 and 2 revealed that some dendrites differed significantly from one another whereas others did not (Fig. 3g, h). No significant difference was observed across the dendrites of neuron 3 (Fig. 3i). Comparing the spine composition on the different dendrites across all cells revealed also the clear difference in spine composition of neurons 1 and 3 (Fig. 3j).

2.5. Differences in spine density across dendrites

Although not systematic, significant differences in spine density could be found between dendrites (Fig. 4a–c). The density of branched spines differed as well across dendrites, but these differences were only rarely significant (Fig. 4d–f). Spine density varied as a function of position along a dendrite, starting low at the proximal end to reach a constant value (medians for the three neurons 1.5, 2.2 and 1.3 spines per micrometer) after 50–100 μm (Fig. 4g–i). This held true for dendrites starting at the soma (Fig. 4g–i, red) and for secondary dendrites (Fig. 4g–i, blue).

2.6. Correlations with local dendrite diameter

We next examined whether spine density and length depend on *local* dendrite diameter and if such correlations are dendrite specific (Fig. 5). We found different correlations, most of them but not all positive. Thick stretches of dendrites tended to have more (Fig. 5a–c) and longer (Fig. 5d–f) spines, though these correlations were not always significant.

2.7. Differences across dendrites persist with simpler quantitative spine descriptors

To complement the clustering analysis with measures that are independent of the hierarchical clustering, we approximated spine morphology using neck diameter, head diameter, their ratio, and spine length (see Methods). Overall, the diameters were well approximated by log-normal distributions (Fig. S4). In all three neurons analyzed, head diameters (Fig. 6a), neck diameters (Fig. 6b), their ratio (Fig. 6c) and spine lengths (Fig. 6d) differed significantly on several dendrites of the same cell. As expected from the clustering results, fewer significant differences were found with neuron 3 than with the other two. Similar differences were found using the total area of the spine (see Methods), the area of the head and that of the neck (Fig. 6e–g), or the variability of the thickness of each spine (expressed as the coefficient of variation of each spine, see Methods) (Fig. 6h–j). As control, we randomly assigned each spine to another dendrite, causing all significant differences to disappear (Fig. S5).

The spine length distributions on each dendrite differed across dendrites (Fig. 7a–c). This was visible even when spines where split in only two groups ("long": ≥3 μm and "short": <3 μm). This revealed a non-homogeneous distribution of spine sizes, with two dendrites on neurons 1 and 2 having many long spines (Fig. 7d–f).

3. Discussion and conclusion

Using superresolution STED microscopy, we showed that most of the dendrites observed in this study possessed a specific set of spine types, even on the same neuron. This might indicate a specialization of individual dendrites for information processing, especially since dendrites can serve as electrophysiologically semi-independent compartments (Larkum et al., 2009). This observation is based on almost 10,000 dendritic spines in three cortical neurons in the turtle *Trachemys scripta elegans*. We examined almost 7000 spines in detail on 31 dendrites. Our analysis covered each neuron almost in its entirety, enabling us to compare the spine compositions of all pairs of dendrites (Fig. 1). Strikingly, we found that each dendrite bore a specific mixture of spine types (Fig. 3); the individuality of each dendrite was expressed in the overall shape and the average length, neck- and head-diameter or surface area of the spines that decorated it (Fig. 6). In two of the three neurons, spine composition differed across dendrites of the same neuron. These differences could not be explained by random distribution of the spine

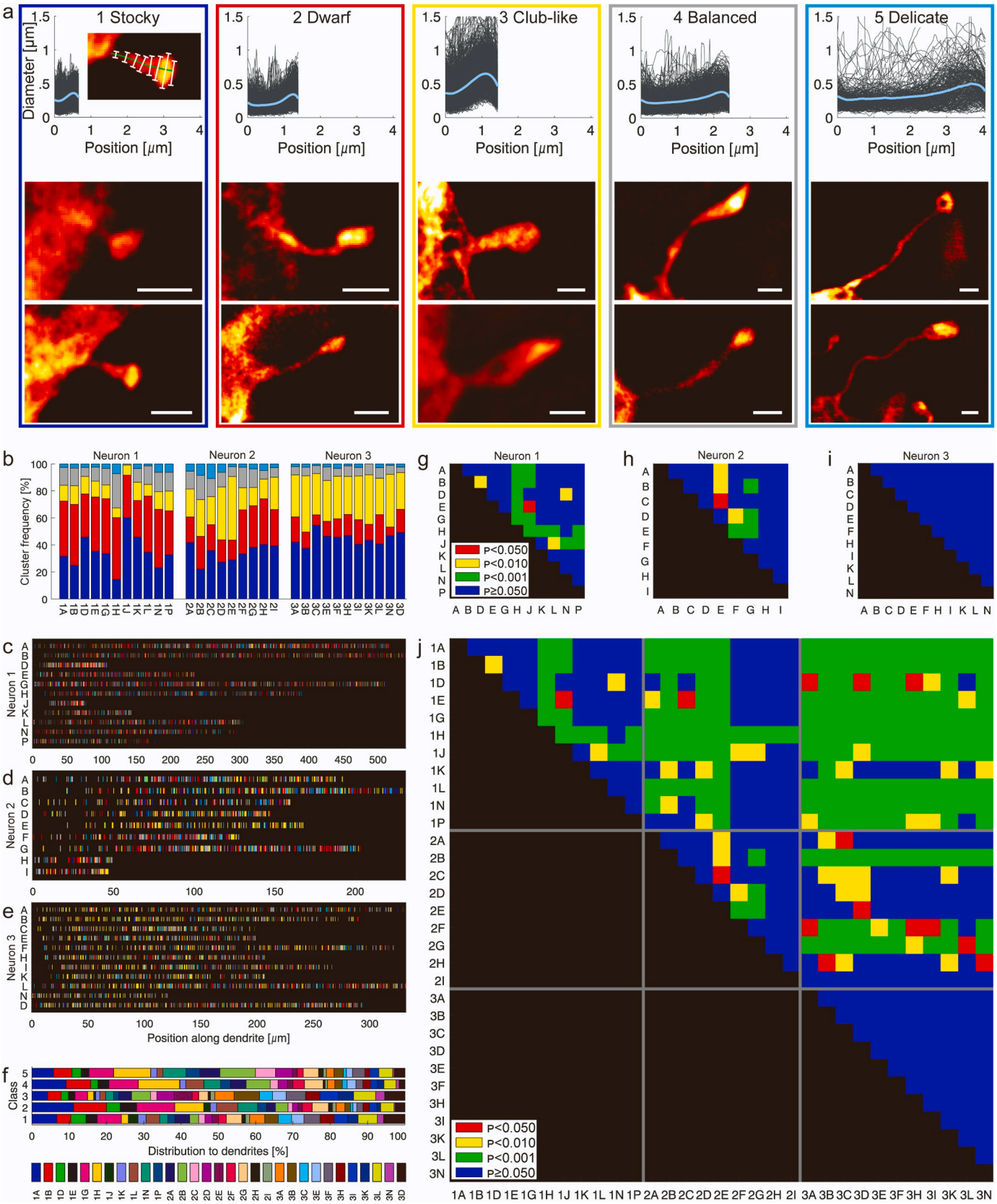

(caption on next page)

Fig. 3. Spines belong to different classes, which are inhomogeneously distributed on the dendrites, (a) 5 classes of spines were identified by hierarchical clustering of shape and length. Upper part of each panel shows the individual diameter profiles (gray) and the average profile of the class (light blue). Positions along the spines are scaled to the average spine length of the respective class. Lower parts show two representative examples of each class. Colored frames correspond to colors in b. Scale bars 500 nm. Inset in the first diagram shows the principle of the diameter measurements (white) perpendicular to the skeleton (green) (in reality programmatically every 20 nm, i. e. finer sampled as indicated here, giving the continuous width profiles shown). (b) Relative frequency of each class on different dendrites, showing a distribution that differs between dendrites. Numbers 1–3 refer to the three neurons, letters to the individual dendrites (cf. Fig. 1). Underlying numbers are tabulated in supplementary table S1. (c–e) Spine classes along dendrites. Each colored line represents one spine, each row one dendrite. Color code as in b. Position is measured from the start of the dendrite. While differences between the dendrites are visible, no clear trend along the dendrites is visible. (f) Repartition of spine classes to dendrites is inhomogeneous. Each color represents one dendrite. The bars show which percentage of spines of a given class are found on which dendrite. (g–j) Pairwise Person's Chi-Square tests show significant differences between the distributions of the clusters on the dendrites: p values color coded: $p \leq 0.05$ red, $p \leq 0.01$ yellow, $p \leq 0.001$ green, $p > 0.05$ blue. All tests have been corrected for multiple comparisons. g–i show the comparsion of dendrites within each cell, j all dendrites across cells, gray lines indicate borders between cells.

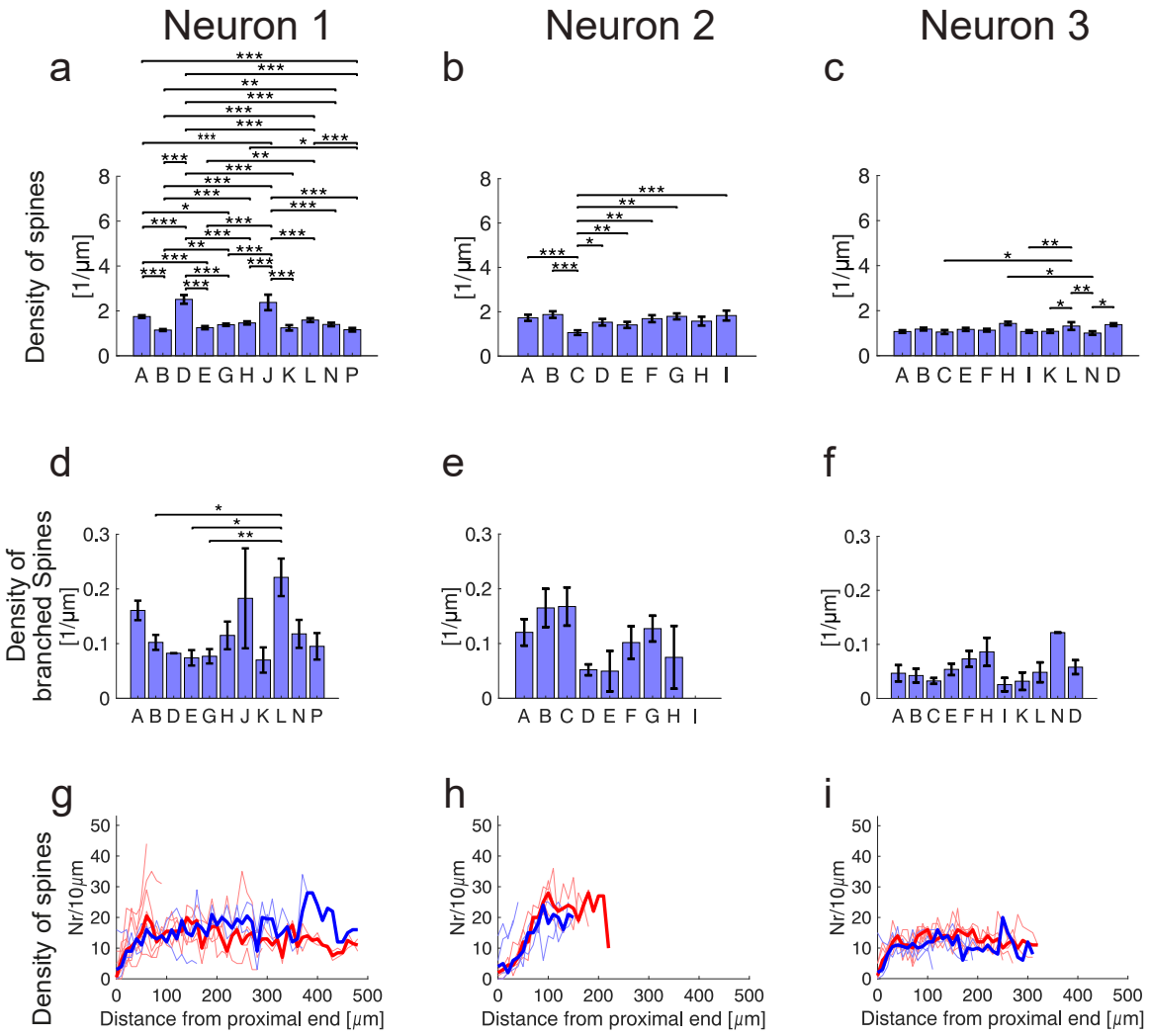

Fig. 4. Spine density varies significantly between several dendrites, (a–c) Spine density is different on different dendrites (bars represent the mean, error bars SEM). (d–f) Density of branched spines is also different; due to generally low numbers of branched spines, theses differences are significant only for some dendrites in the first cell. * $p \leq 0.05$, ** $p \leq 0.01$, *** $p \leq 0.001$. (g–i) Spine density increases on almost all dendrites from the proximal end over the first 50–100 µm to become then relatively constant. Primary dendrites (red) show always this density profile, while side branches (blue) show it often but not always. Thick lines represent the median, thin lines individual dendrites.

types across dendrites. In addition, a clear difference was seen between cells.

A specific composition of the spines on each dendrite has to our knowledge only been published as a coarse distinction for basal/apical dendrites of pyramidal cells (Benavides-Piccione et al., 2013), although dendrite-specific function has been demonstrated in different contexts: Otor et al. demonstrated recently functional compartimentalization in tuft dendrites of layer 5 pyramidal neurons in murine motor cortex (Otor et al., 2022). They found that motor variables were differentially represented in different tuft tree segments. If the individuality of dendrites observed there is due to specific inputs or due to intrinsic properties of the dendrites like spine types decorating them, remains unclear. Homeostatic spine scaling localized to individual dendrites has been reported in visual cortex of mice after monocular enucleation (Barnes et al., 2017). In primary somatosensory cortex of mice, pyramidal neurons' excitatory and inhibitory synapses are weighted toward the same dendritic segments; large inhibitory synapses were seen to be present more on some dendrites than on others, whereas this was not the case for

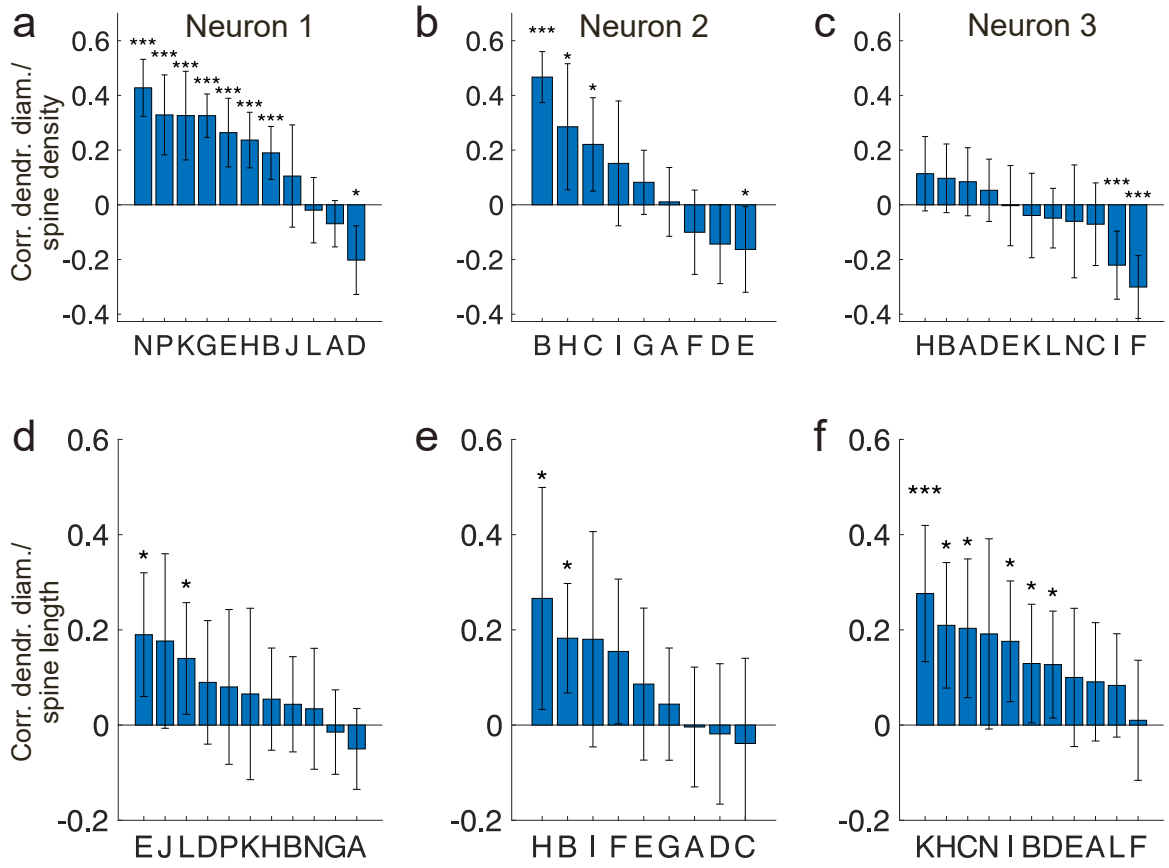

Fig. 5. Spine parameters correlate with dendrite diameter, (a–c) The local dendrite diameter is often correlated with the local density of spines, especially in the first neuron. Clear differences are visible between the neurons. (d–f) The spine length is sometimes positively correlated with the local diameter of the dendrite. Error bars show 95% confidence intervals of the Pearson correlation coefficients. * $p \leq 0.05$, ** $p \leq 0.01$, *** $p \leq 0.001$.

large spines (Iascone et al., 2020).

The differences in shape and size across spines (Figs. 2, 3) may have an impact on the synaptic connections which they represent. Since the volume of a spine head is proportional to the cube of its diameter and the area of the post-synaptic density is strongly correlated with spine volume, connection strengths may vary greatly across synapses (Borczyk et al., 2019). Indeed, differences in spine shape alter electrical, diffusional and biochemical properties (Harris and Stevens, 1988; Harris and Stevens, 1989; Yuste and Denk, 1995; Yuste et al., 2000; Nusser et al., 2001), thus affecting synaptic strength and learning (Araya et al., 2014).

Some dendrites were decorated with many long spines (Fig. 1, 7). This suggests that such dendrites may sample a larger volume of possible synaptic inputs, while potentially contributing weakly to depolarization due to high neck resistance (Yuste, 2013).

Mammalian spines are commonly classified into few categories (“thin”, “mushroom”, “stubby” and “filopodia”) (Benavides-Piccione et al., 2013), although this classification probably represents the coarse binning of a continuum (Arellano et al., 2007; Pchitskaya and Bezprozvanny, 2020). Likewise our clustering of turtle spines should be seen as a binning of a continuum of shapes. Notably, clustering of a continuum is considered to describe the data better than a classification into predefined groups (Pchitskaya and Bezprozvanny, 2020).

Spine density as a function of distance from the soma (Fig. 4) followed closely the distribution that was found in electron-microscopy studies in rat (Wilson et al., 1983), cat (Kemp and Powell, 1971), and human (Benavides-Piccione et al., 2013). It thus seems to be an evolutionarily conserved principle.

We found significant, but not very strong correlations of spine density and length with dendrite diameter (Fig. 5).

Chemical fixation (as used here) was found by Tamada et al. to impact especially the spine neck diameter (Tamada et al., 2020), whereas they did not see significant differences in spine head volume and spine length compared to cryofixation in their electron-microscopy study. This might influence the absolute values that we determine for the neck diameters (Fig. 6) and to a certain extent the overall spine shapes, especially in the neck regions. Such potential fixation artifacts would affect all spines. It is therefore very unlikely that they would artificially introduce inhomogeneous distribution of spine classes on different dendrites. This assumption is supported by the differences in spine length, which are large compared to neck diameters and less prone to chemical fixation artifacts (Tamada et al., 2020). Fixation artifacts (Tamada et al., 2020) might also affect the dendrite diameter. It is expected that such artifacts would be independent of local spine properties and therefore would not introduce artifactual correlations of dendrite diameter with spine length and density.

We found that 0.8% of spines have a complex shape, with spinules protruding from the head (Fig. 2). In reptiles (*Anolis carolinesis*) Waxman et al. reported small (<200 nm) protrusions from pre- into postsynaptic profiles (Waxman et al., 1980). In rodents, it was reported that such spinules might project into presynaptic boutons and serve for trans-endocytosis and retrograde signaling (Spacek and Harris, 2004; Zaccard et al., 2020). GluA1 receptors have a higher mobility in spinules compared to the rest of the spine in cultured hippocampal neurons (Inavalli et al., 2019). Spacek et al. report that spinules reach also into astrocytic processes; this might be indicative of direct communication between perisynaptic glia and spines (Spacek and Harris, 2004). The fraction of spinule-expressing spines in turtle cortex was much lower than in rat hippocampus, in which Spacek and Harris report spinules on

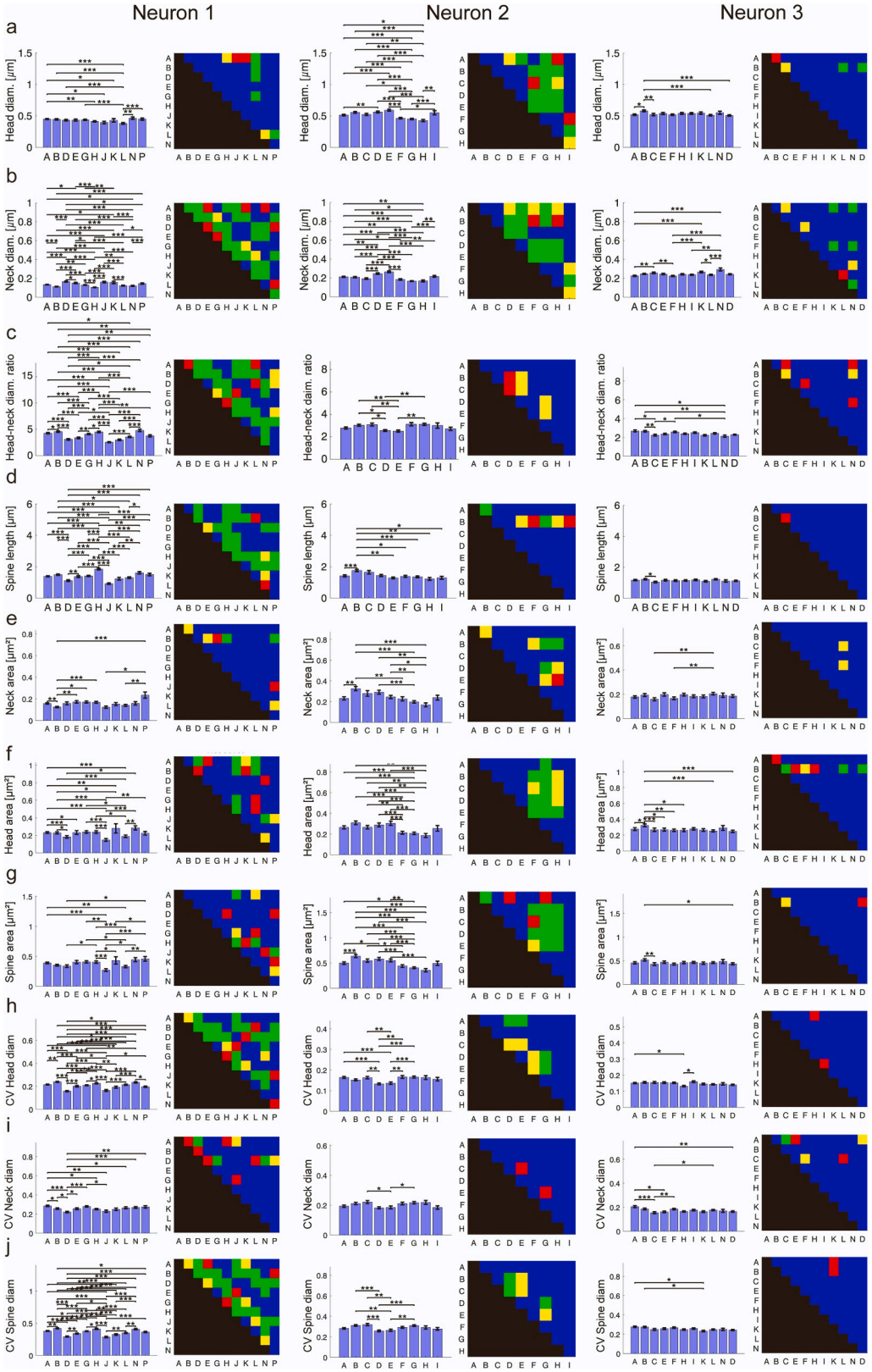

Fig. 6. Spine characteristics vary on different dendrites, Spine parameters are significantly different on dendrites of all neurons (cf. Fig. 1 for their images). Bar charts show mean ± SEM; Matrices show p values of mutual comparisons $p \leq 0.05$ red, $p \leq 0.01$ yellow, $p \leq 0.001$ green, $p > 0.05$ blue. In bar charts: * $p \leq 0.05$, ** $p \leq 0.01$, *** $p \leq 0.001$. All tests have been corrected for multiple comparisons (Kruskal-Wallis test). Each colum represents one neuron. All tested parameters differ significantly between several dendrites: (a) Head diameter, (b) Neck diameter, (c) Ratio of head diamter to neck diameter, (d) Spine length, (e–g) neck, head, spine areas, (h–j) width variablity within spines given as coefficient of variation (CV).

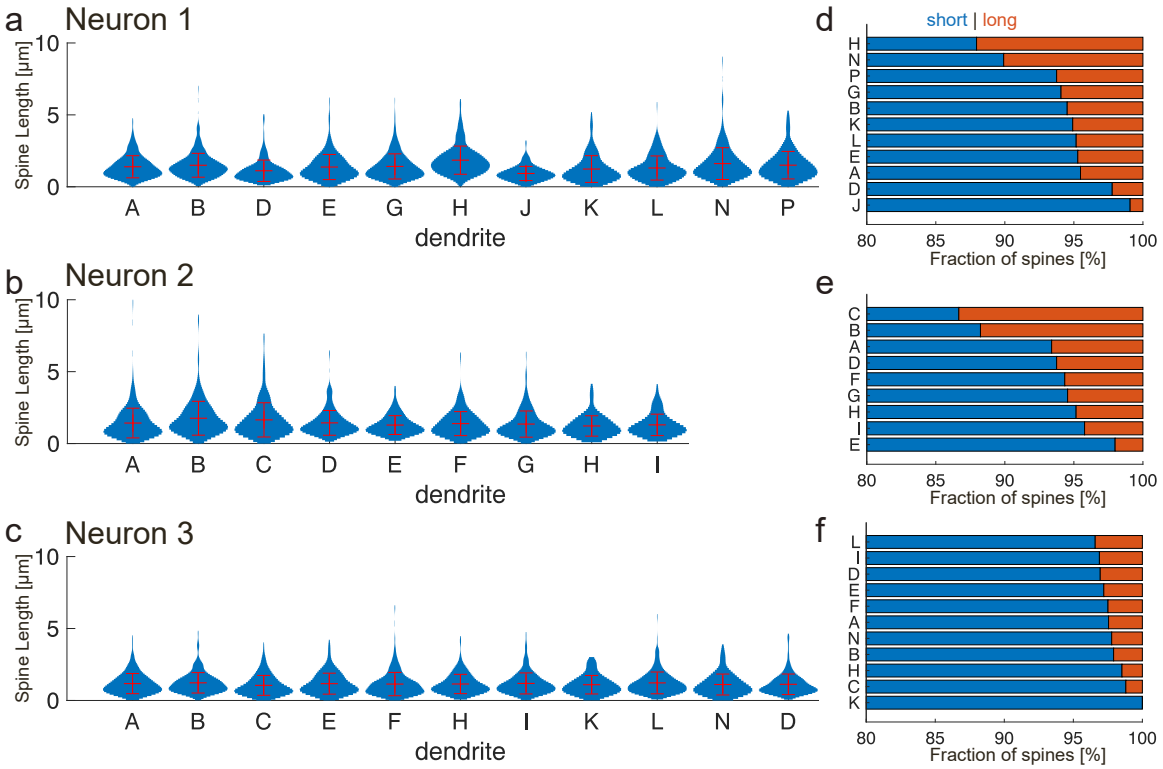

Fig. 7. Spine length varies between dendrites, (a–c) The length of spines is differently distributed on different dendrites on all neurons (violin plots, red crosses ± error bars: means ± SD. (d–f) A condensed representation assigning spines to a "short" (blue, < 3 µm) or "long" (orange, ≥ 3 µm) group shows that the abundance of these groups differs on all dendrites and on neuron 3 less than on the others.

32% of all spines (45 out of 139 spines) (Spacek and Harris, 2004). Also Zaccard et al. report, for dissociated cortical pyramidal murine neurons, a higher fraction of spines that have (at least transiently) spinules (85% on mushroom spines) (Zaccard et al., 2020). This major difference with our study may result from the fact that Zaccard et al. observed many short-lived spinules (70% less than 60 s) over a period of 1000 s, while our data are snapshots from fixed tissue.

Five percent of the spines analyzed were branched, matching the proportion of branched spines in medium spiny neurons from dorsolateral striatum in *Trachemys scripta elegans* (González et al., 2013). In rat Purkinje cells, the fraction of branched spines is 2.2% as seen with high-voltage electron microscopy of Golgi impregnated samples (Lee et al., 2004). The fraction of branched spines seems to increase after induction of long-term potentiation (LTP), at least in the rat hippocampus, where an increase from 2.5% to 6% (Dhanrajan et al., 2004) or from 1.7% to 5.5% (Trommald et al., 1996) were observed. Branched spines may thus reflect ongoing plasticity and differentiation in adults (Lee et al., 2005).

Our most interesting result concerns the correlation of spine types as well as spine density with individual dendrites (Figs. 3 and 4). Also quantitative spine parameters like lengths and diameters differ between dendrites (Fig. 6). Electron microscopy studies examined, in mammalian hippocampus and cerebral cortex, the sizes of synaptic contacts formed by the same axon onto a same postsynaptic neuron, hypothesizing that Hebbian plasticity rules should lead to a correlation between the sizes of such converging contacts. They found such correlations to be significant (Motta et al., 2019; Bloss et al., 2018; Sorra and Harris, 1993). Following a similar reasoning, our results, which point to dendritic compartments defined by spine composition, suggest that turtle-cortex dendrites could form relatively uniform electrical compartments — thus linking the fate of synapses placed on them. The shape of spines is critical for their electric/synaptic properties (Araya et al., 2014). Spine volumes are in rodents strongly correlated with the size of the post synaptic density, presynaptic active zone size and the number of docked vesicles (Schikorski and Stevens, 1999); the calcium dynamics in spines depends on their neck length (Holthoff et al., 2002). Gidon et al. found heterogeneous activation functions of human Layer 2/3 dendrites (Gidon et al., 2020). Based on their turtle-dendrite electrophysiological recordings Larkum et al. reported that some neurons may possess less active dendrites (Larkum et al., 2008). Since they could record only from one dendrite per neuron, this could mean that some dendrites of one and the same neuron are less active than others of the same cell. This would be consistent with our morphological data, suggestive of large dendritic compartments. Branco et al. showed that the dendrites of rat pyramidal cells can act as processing compartments (Branco et al., 2010); dendrite-specific spine composition might tune such computations. It remains unclear, however, whether the different spine morphologies we observed represent functional differences.

In conclusion, this study showed with superresolution microscopy a large variety of dendritic spines in turtle cortex, including various spinules and branched spines with different branching patterns. These spinules might serve for retrograde signaling to the presynaptic neuron but also to glia. Branched, multi-headed spines may reflect ongoing plasticity and differentiation but also postsynapses engulfed by the presynaptic terminal.

Most importantly, we demonstrated that different dendrites from the same neuron could be decorated by different spine types. This points to dendritic compartments defined by spine composition with potentially functional roles of individual dendrites and suggests mesoscopic organization of dendrites in this system.

4. Materials and methods

4.1. Animals and tissue preparation

The procedures involving animal husbandry and care were

conducted in conformity with the institutional guidelines that are in compliance with national German and international laws and policies (DIRECTIVE 2010/63/EU; Tierschutzgesetz; Tierschutz-Versuchstier-Verordnung; FELASA guidelines). The animals were sacrificed according to § 4 (3) Tierschutzgesetz, and § 2 Tierschutz-Versuchstier-Verordnung.

Cortical slabs were prepared and single neurons were patched as described in (Hemberger et al., 2019): Wild-type turtles (*Trachemys scripta elegans*) were obtained from an open-air breeding facility (NASCO Biology, WI, USA). Turtles were anesthetized with dexdomitor (75 µg/kg, IM) and ketamine (23 mg/kg, IM). Turtles were decapitated after loss of the corneal reflex. The heads were rapidly transferred into turtle ACSF solution (96.5 mM NaCl, 2.6 mM KCl, 4 mM $CaCl_2$, 2 mM $MgCl_2$, 31.5 mM $NaHCO_3$, 20 mM glucose, pH 7.4) bubbled with carbogen (95% O_2, 5% CO_2). The skull was opened; dura mater and arachnoid were removed. To prepare cortical slabs the cortical sheet was cut with iridectomy scissors as follows: (1) transversally: slightly posterior to the anterior pole of the cerebral cortex; (2) transversally: 5–7 mm caudal to the first incision; (3) parasagitally: along the border between medial and dorsal cortices medially; (4) just slightly before where dorsal cortex merges with the dorso-ventricular ridge (DVR). During patching at room temperature (about 23 °C) the slabs were constantly perfused with turtle ACSF, bubbled with carbogen, with a flow rate of 2–6 ml/min.

4.2. Staining

Neurons from two turtles (Neuron 1 and 2: male, 275 g; Neuron 3: male, 330 g) were filled with biocytin via patch pipettes: Long-shank patch pipettes (6–8 MΩ) were pulled with a Sutter P1000 electrode puller from borosilicate glass (Science Products BF150–86–10, outer diameter 1.50 mm, inner diameter 0.86 mm). Pipettes were filled with internal solution (140 mM K-gluconate, 4 mM NaCl, 14 mM Phosphocreatine, 10 mM HEPES, 4 mM Mg-ATP, 0.3 mM Na-GTP, 4 mg/ml Biocytin, 0.015 mM Alexa 488). Experiments were carried out on an upright Nikon microscope with 16x water-immersion objective. Cells were patched for at least 20 min to ensure filling with biocytin. Proper filling was verified by observing the increasing fluorescence of Alexa 488 in the neuron.

Only one cell per slab was filled with biocytin. After retraction of the patch pipette, the slabs were immediately fixed for 24 h in 100 mM phosphate buffer (PB) (pH 7.4) with 4% paraformaldehyde at 4 °C.

Patched neurons were stained capitalizing on the strong binding of streptavidin to biocytin: After 3x washing in PB cortical slabs were incubated for 1 h in 3% hydrogen peroxide, 4x washed in PB, incubated for 1 h in 2% Triton X-100 in PBS for permeabilization and subsequently incubated over night at 4 °C in 0.1% Triton X-100 in PBS containing 0.016 g/l streptavidin coupled to the fluorophore Atto 647 N (Atto Tec, Siegen, Germany). Slabs were rinsed three times for 1 h in PBS and mounted in Mowiol or Aqua Polymount on coverslips #1.5, ventricular side to the cover slip.

4.3. STED Microscopy

Slabs were imaged on an inverted STED Microscope (Expert Line, Abberior Instruments, Göttingen, Germany) with an 100x silicon oil immersion objective (UPLSAPO100XS, Olympus Germany, Hamburg, Germany) and a toroidal ("donut") depletion pattern of the STED focus. Wavelengths: Excitation 640 nm, STED 775 nm, detection 650–720 nm; voxel size $20\times20\times300$ nm^3. Image stacks were planewise linearly deconvoved (Wiener filtered) using theoretical point spread functions and custom-written routines in Matlab (The Mathworks, Natick, USA).

The neurons with the wide ramifications of the dendrites were imaged piecewise, following individual dendrites as identified in overview images, with small overlap between the individual STED stacks. Overview images were recorded on the same microscope in confocal mode with a 30x silicon oil immersion objective (Olympus UPLSAPO30XS) and stitched together with the ImageJ plugin "Pairwise Stitching" (Preibisch et al., 2009).

4.4. Skeletonization, segmentation and spine profiles

Unless otherwise noted, all analysis was performed with custom-written routines in Matlab. Skeletons of dendrites and spines were determined manually in the 3D data sets using the software webKnossos (Boergens et al., 2017). First, skeletons of all spines and the dendrite in each individual image stack were marked. The skeletons of the dendrites in individual image stacks were subsequently joined using custom-written routines in Matlab. In spine-skeletons attachment points to the dendrite, end of the neck, start of the head and end of the spine were marked manually. Where present, start and end of spinules were marked, too. In cases where the full spine was not clearly visible, only the head position was marked. These "single-point" spineheads (2935 in total) were included in statistics that are based exclusively on spine positions (e.g. spine density, Fig. 4), but obviously not used for clustering, length measurements etc.

Segmentation was based on the deconvolved 3D data sets in combination with the skeletons. Each spine was manually segmented along the skeleton in the imaging plane (xy). Due to the lower resolution along the optical axis (z), no attempt was made for a volume reconstruction. However, the xy segmentation follows the spine across several z-planes.

Diameter profiles of the spines were determined by calculating the diameter of the segmented spine perpendicularly to the skeleton about every 20 nm.

4.5. Spine parameters

Quantitative spine parameters (Fig. 6) were specified as follows: "Head diameter" was defined as the largest diameter within the head region, "neck diameter" as the smallest diameter in the neck region, "spine length" as the length along the 3D skeleton from the attachment point to the end of the head. Head-neck diameter ratio for each spine as the quotient of its head diameter and neck diameter.

Spine, neck and head area were defined as the sum over all diameter profiles times the actual sampling interval, i.e. essentially as the integral of the diameter values along the length of the spine. Of note, these areas were not calculated as a 2D projection but used the segmentation in 3D.

The diameter variations were calculated as the coefficient of variation of all diameter values in each spine (respectively the neck and head regions). They represent the diameter variation *within* each spine, not between spines.

Spine densities were determined from the distance of each spine head to its nearest neighbor. According error bars were obtained from the variation in these distances. For display (Fig. 4), the densities were converted to the more common spine density (the inverse of the intervals). The error on the density was calculated via error propagation to be the error of the intervals divided by the squared mean interval. For correlations of spine density with local dendrite diameter, the number of spines in a segment of 3 µm length around each spine was counted.

4.6. Clustering

Spines were clustered based on their diameter profile and length. To disentangle the diameter profile (measured every ~20 nm) from the spine length, the profiles were resampled to contain 100 sampling points for every spine, so that shape served as a clustering criterion independently from length. Length was then included in the clustering as an independent feature.

Hierarchical clustering with the Ward algorithm and Euclidean distances was used in a multidimensional space. Dimensions 1–100 represented the diameter of the spine from attachment point to its end, dimensions 101–200 the length (repeated 100 times to give it a balanced

weight compared to the 100 diameter values). To balance the influence of the different dimensions during clustering, the length values were scaled so that the mean rescaled length matches the mean diameter. Hierarchical clustering needs setting of a cutoff threshold that determines in how many clusters the data set is split. This threshold was determined according to the Davies-Bouldin Criterion. The Davies-Bouldin (DB) index is defined as $DB = \frac{1}{k}\sum_{i=1}^{k}\max_{j\neq i}(D_{(i,j)})$, with $D_{(i,j)}$ being the in-cluster to inter-cluster distance ratio of clusters i and j, i.e. $D_{i,j} = \frac{(\bar{d}_i+\bar{d}_j)}{d_{i,j}}$. $\bar{d}_i$ represents the mean Euclidian distance between each point in cluster i and the centroid of that cluster, analogous for $\bar{d}_j$. $d_{i,j}$ represents the Euclidean distance between the centers of clusters i and j. Different cutoff thresholds are tested, leading to different numbers of clusters k. For the optimal clustering solution the Davies-Bouldin (DB) index is lowest.

For display of typical diameter profiles (Fig. 3), the length of all profiles within each cluster were scaled to the mean length.

For display of spine classes along the dendrite (Fig. 3c–e), one bar represents 0.5 μm dendrite length. If more than one spine is present within this dendrite-stretch, the color displayed represents the majority of spine classes.

4.7. Statistics

Statistical differences between multiple groups (e.g. multiple dendrites, Fig. 4, Fig. 6) were evaluated with a Kruskal-Wallis test at a 5% significance level. Matlab was used for all statistical tests. As control (Fig. S5), all spines were assigned to a random dendrite, while the original number of spines on each dendrite was kept.

Bar graphs in Figs. 4 and 6 represent mean ± standard error of the mean (SEM).

Correlations between different spine characteristics (Fig. S1) were calculated as Pearson's coefficient (Matlab function corrcoef) and tested for rejection of the null-hypothesis (no correlation) at a 5% significance level, which is equivalent to the fact that the 95% confidence interval does not include zero.

To test for significant differences of cluster distribution on dendrites (Fig. 3) Person's Chi Square tests were performed with Matlab (function crosstab) with a 5% significance level. A conservative correction for multiple comparisons was applied, using Bonferroni correction with the number of all mutual comparisons (465) for all cells, even where only dendrites within one cell are shown (Fig. 3g–i). Where the matrices in Fig. 3g–j are green, yellow or red, the respective dendrites are significantly different in terms of spine classes.

Declaration of Competing Interest

The authors declare that they have no known competing financial interests or personal relationships that could have appeared to influence the work reported in this paper.

Data Availability

Data will be made available on request.

Acknowledgments

We thank Michaela Klinkmann for excellent help with the surgeries, Anja Arends, Ángeles Macias Pardo, Theres Manthey, and Christina Thum for excellent technical assistance, Emily Northrup, Gabriela Wexel and their team for reliable animal care, Moritz Helmstaedter, Heiko Wissler, Alessandro Motta and Norman Rzepka for access to and help with webKnossos, Miriam Kunz for help with tracing and segmentation, the team from Abberior Instruments for superb customer support, Hermann Cuntz and Claudia Schirra for helpful discussions. This work was supported by a grant of the Deutsche Forschungsgemeinschaft (DFG), SFB 894.

Appendix A. Supporting information

Supplementary data associated with this article can be found in the online version at doi:10.1016/j.pneurobio.2023.102541.

References

Araya, R., Vogels, T.P., Yuste, R., 2014. Activity-dependent dendritic spine neck changes are correlated with synaptic strength. Proc. Natl. Acad. Sci. USA 111 (28), E2895–E2904. https://doi.org/10.1073/pnas.1321869111. ISSN 0027-8424, 1091-6490. http://www.pnas.org/cgi/doi/10.1073/pnas.1321869111.

Arellano, Jon I., Benavides-Piccione, Ruth, DeFilipe, Javier, Yuste, Rafael, 2007. Ultrastructure of dendritic spines: correlation between synaptic and spine morphologies. Front. Neurosci. 1 (1), 131–143. https://doi.org/10.3389/neuro.01.1.1.010.2007. ISSN 16624548. http://journal.frontiersin.org/article/10.3389/neuro.01.1.1.010.2007/abstract.

Ballesteros-Yáñez, I., Benavides-Piccione, R., Elston, G.N., Yuste, R., DeFelipe, J., 2006. Density and morphology of dendritic spines in mouse neocortex. Neuroscience 138 (2), 403–409. https://doi.org/10.1016/j.neuroscience.2005.11.038. ISSN 03064522. https://linkinghub.elsevier.com/retrieve/pii/S0306452205013199.

Barnes, Samuel J., Franzoni, Eleonora, Jacobsen, R.Irene, Erdelyi, Ferenc, Szabo, Gabor, Clopath, Claudia, Keller, Georg B., Keck, Tara, 2017. Deprivation-induced homeostatic spine scaling in vivo is localized to dendritic branches that have undergone recent spine loss. Neuron 96 (4), 871–882. https://doi.org/10.1016/j.neuron.2017.09.052.

Philipp Bastians. *Comparative cortical connectomics: three-layered cortex in mouse and turtle*. Phd thesis, Ludwig-Maximilians-Universität München, September 2018. URL http://nbn-resolving.de/urn:nbn:de:bvb:19–229269.

Benavides-Piccione, Ruth, Fernaud-Espinosa, Isabel, Robles, Victor, Yuste, Rafael, DeFelipe, Javier, 2013. Age-based comparison of human dendritic spine structure using complete three-dimensional reconstructions. Cereb. Cortex 23 (8), 1798–1810. https://doi.org/10.1093/cercor/bhs154. ISSN 1460-2199, 1047-3211. https://academic.oup.com/cercor/article-lookup/doi/10.1093/cercor/bhs154.

Bloss, Erik B., Cembrowski, Mark S., Karsh, Bill, Colonell, Jennifer, Fetter, Richard D., Spruston, Nelson, 2018. Single excitatory axons form clustered synapses onto CA1 pyramidal cell dendrites. Nat. Neurosci. 21 (3), 353–363. https://doi.org/10.1038/s41593-018-0084-6.

Boergens, Kevin M., Berning, Manuel, Bocklisch, Tom, Bräunlein, Dominic, Drawitsch, Florian, Frohnhofen, Johannes, Herold, Tom, Otto, Philipp, Rzepka, Norman, Werkmeister, Thomas, Werner, Daniel, Wiese, Georg, Wissler, Heiko, Helmstaedter, Moritz, 2017. webKnossos: efficient online 3D data annotation for connectomics. Nat. Methods 14 (7), 691–694. https://doi.org/10.1038/nmeth.4331. ISSN 1548-7091, 1548-7105. http://www.nature.com/articles/nmeth.4331.

Boergens, Kevin M., Kapfer, Christoph, Helmstaedter, Moritz, Denk, Winfried, Borst, Alexander, 2018. Full reconstruction of large lobula plate tangential cells in drosophila from a 3d EM dataset. PLOS ONE 13 (11), e0207828. https://doi.org/10.1371/journal.pone.0207828.

Borczyk, Malgorzata, Alicja Sliwinska, Magorzata, Caly, Anna, Bernas, Tytus, Radwanska, Kasia, 2019. Neuronal plasticity affects correlation between the size of dendritic spine and its postsynaptic density. Sci. Rep. 9 (1), 1693 https://doi.org/10.1038/s41598-018-38412-7. ISSN 2045-2322. http://www.nature.com/articles/s41598-018-38412-7.

Branco, Tiago, Clark, Beverley A., Häusser, Michael, 2010. Dendritic discrimination of temporal input sequences in cortical neurons. Science 329 (5999), 1671–1675. https://doi.org/10.1126/science.1189664. https://www.science.org/doi/abs/10.1126/science.1189664.

Davies, David L., Bouldin, Donald W., 1979. A cluster separation measure. IEEE Trans. Pattern Anal. Mach. Intell. PAMI-1 (2), 224–227. https://doi.org/10.1109/TPAMI.1979.4766909.

DeFelipe, Javier, Fariñas, Isabel, 1992. The pyramidal neuron of the cerebral cortex: morphological and chemical characteristics of the synaptic inputs. Prog. Neurobiol. 39 (6), 563–607. https://doi.org/10.1016/0301-0082(92)90015-7. ISSN 03010082. https://linkinghub.elsevier.com/retrieve/pii/0301008292900157.

Denk, Winfried, Horstmann, Heinz, 2004. Serial block-face scanning electron microscopy to reconstruct three-dimensional tissue nanostructure. PLOS Biol. 2 (11), e329 https://doi.org/10.1371/journal.pbio.0020329. https://doi.org/10.1371/journal.pbio.0020329.

Dhanrajan, Tiruchinapalli M., Lynch, Marina A., Kelly, Aine, Popov, Victor I., Rusakov, Dmitri A., Stewart, Michael G., 2004. Expression of long-term potentiation in aged rats involves perforated synapses but dendritic spine branching results from high-frequency stimulation alone. Hippocampus 14 (2), 255–264. https://doi.org/10.1002/hipo.10172.

Dunaevsky, Anna, Tashiro, Ayumu, Majewska, Ania, Mason, Carol, Yuste, Rafael, 1999. Developmental regulation of spine motility in the mammalian central nervous system. Proc. Natl. Acad. Sci. USA 96 (23), 13438–13443. https://doi.org/10.1073/pnas.96.23.13438.

Ebner, Ford F., Colonnier, Marc, 1975. Synaptic pattern in the visual cortex of turtle: an electron microscopic study. J. Comp. Neurol. 160 (1), 51–80. https://doi.org/10.1002/cne.901600105.

Elston, Guy N., Benavides-Piccione, Ruth, DeFelipe, Javier, 2001. The pyramidal cell in cognition: a comparative study in human and monkey. J. Neurosci. 21 (17), RC163. https://doi.org/10.1523/JNEUROSCI.21-17-j0002.2001. ISSN 0270-6474, 1529-2401.

Fournier, Julien, Müller, Christian M., Schneider, Ingmar, Laurent, Gilles, 2018. Spatial information in a non-retinotopic visual cortex. Neuron 97 (1), 164–180.e7. https://doi.org/10.1016/j.neuron.2017.11.017.

Gao, Ruixuan, Asano, Shoh M., Upadhyayula, Srigokul, Pisarev, Igor, Milkie, Daniel E., Liu, Tsung-Li, Singh, Ved, Graves, Austin, Huynh, Grace H., Zhao, Yongxin, Bogovic, John, Colonell, Jennifer, Ott, Carolyn M., Zugates, Christopher, Tappan, Susan, Rodriguez, Alfredo, Mosaliganti, Kishore R., Sheu, Shu-Hsien, Pasolli, H.Amalia, Pang, Song, Xu, C.Shan, Megason, Sean G., Hess, Harald, Lippincott-Schwartz, Jennifer, Hantman, Adam, Rubin, Gerald M., Kirchhausen, Tom, Saalfeld, Stephan, Aso, Yoshinori, Boyden, Edward S., Betzig, Eric, 2019. Cortical column and whole-brain imaging with molecular contrast and nanoscale resolution. ISSN 0036-8075, 1095-9203 Science 363 (6424), eaau8302. https://doi.org/10.1126/science.aau8302. ISSN 0036-8075, 1095-9203. https://www.sciencemag.org/lookup/doi/10.1126/science.aau8302.

Gidon, Albert, Zolnik, Timothy Adam, Fidzinski, Pawel, Bolduan, Felix, Papoutsi, Athanasia, Poirazi, Panayiota, Holtkamp, Martin, Vida, Imre, Larkum, Matthew Evan, 2020. Dendritic action potentials and computation in human layer 2/3 cortical neurons. Science 367 (6473), 83–87. https://doi.org/10.1126/science.aax6239.

Goncharova, N.V., Davydova, T.V., 1983. Phylogenetic and ecological features of the structural organization of the forebrain cortical plate in Chelonia: 1. neuronal composition and dendrite spines of the cortical zones in land and aquatic Chelonia. J. für Hirnforsch. 24 (3), 253–266. http://europepmc.org/abstract/MED/6886394.

González, Carolina, Mendoza, Janeth, Avila-Costa, MarÃ.-a Rosa, Arias, Juan M., Barral, Jaime, 2013. Golgi study of medium spiny neurons from dorsolateral striatum of the turtle Trachemys scripta elegans. Neurosci. Lett. 556, 227–231. https://doi.org/10.1016/j.neulet.2013.10.044. ISSN 03043940. https://linkinghub.elsevier.com/retrieve/pii/S0304394013009488.

Harris, Km, Stevens, Jk, 1988. Dendritic spines of rat cerebellar Purkinje cells: serial electron microscopy with reference to their biophysical characteristics. J. Neurosci. 8 (12), 4455–4469. https://doi.org/10.1523/JNEUROSCI.08-12-04455.1988. ISSN 0270-6474, 1529-2401.

Harris, Km, Stevens, Jk, 1989. Dendritic spines of CA 1 pyramidal cells in the rat hippocampus: serial electron microscopy with reference to their biophysical characteristics. J. Neurosci. 9 (8), 2982–2997. https://doi.org/10.1523/JNEUROSCI.09-08-02982.1989. ISSN 0270-6474, 1529-2401.

Hell, S.W., 2007. Far-field optical nanoscopy. Science 316 (5828), 1153–1158. https://doi.org/10.1126/science.1137395.

Hell, S.W., Wichmann, J., 1994. Breaking the diffraction resolution limit by stimulated emission: stimulated-emission-depletion fluorescence microscopy. Opt. Lett 19 (11), 780–782. https://doi.org/10.1364/OL.19.000780.

Hemberger, Mike, Shein-Idelson, Mark, Pammer, Lorenz, Laurent, Gilles, 2019. Reliable sequential activation of neural assemblies by single pyramidal cells in a three-layered cortex. Neuron 104 (2), 353–369. https://doi.org/10.1016/j.neuron.2019.07.017 e5. https://linkinghub.elsevier.com/retrieve/pii/S0896627319306439.

Holthoff, Knut, Tsay, David, Yuste, Rafael, 2002. Calcium dynamics of spines depend on their dendritic location. Neuron 33 (3), 425–437. https://doi.org/10.1016/S0896-6273(02)00576-7.

Iascone, Daniel Maxim, Li, Yujie, Sümbül, Uygar, Doron, Michael, Chen, Hanbo, Andreu, Valentine, Goudy, Finola, Blockus, Heike, Abbott, Larry F., Segev, Idan, Peng, Hanchuan, Polleux, Franck, 2020. Whole-neuron synaptic mapping reveals spatially precise excitatory/inhibitory balance limiting dendritic and somatic spiking. Neuron 106 (4), 566–578. https://doi.org/10.1016/j.neuron.2020.02.015 e8.

Inavalli, V.V.G.Krishna, Lenz, Martin O., Butler, Corey, Angibaud, Julie, Compans, Benjamin, Levet, Florian, Tønnesen, Jan, Rossier, Olivier, Giannone, Gregory, Thoumine, Olivier, Hosy, Eric, Choquet, Daniel, Sibarita, Jean-Baptiste, Nägerl, U.Valentin, 2019. A super-resolution platform for correlative live single-molecule imaging and STED microscopy. Nat. Methods 16 (12), 1263–1268. https://doi.org/10.1038/s41592-019-0611-8.

Jacobs, B., 2001. Regional dendritic and spine variation in human cerebral cortex: a quantitative Golgi study. Cereb. Cortex 11 (6), 558–571. https://doi.org/10.1093/cercor/11.6.558. ISSN 14602199.

Kasai, Haruo, Fukuda, Masahiro, Watanabe, Satoshi, Hayashi-Takagi, Akiko, Noguchi, Jun, 2010. Structural dynamics of dendritic spines in memory and cognition. Trends Neurosci. 33 (3), 121–129. https://doi.org/10.1016/j.tins.2010.01.001. https://www.sciencedirect.com/science/article/pii/S0166223610000020.

Kemp, Janet M., Powell, T.P.S., 1971. The termination of fibres from the cerebral cortex and thalamus upon dendritic spines in the caudate nucleus: a study with the Golgi method. Philos. Trans. R. Soc. Lond. Ser. B 262 (845), 429–439. https://doi.org/10.1098/rstb.1971.0105.

Konur, Sila, Rabinowitz, Daniel, Fenstermaker, Vivian L., Yuste, Rafael, 2003. Systematic regulation of spine sizes and densities in pyramidal neurons. J. Neurobiol. 56 (2), 95–112. https://doi.org/10.1002/neu.10229. ISSN 0022-3034, 1097-4695.

Larkum, M.E., Nevian, T., Sandler, M., Polsky, A., Schiller, A., 2009. Synaptic integration in tuft dendrites of layer 5 pyramidal neurons: A new unifying principle. Science 325 (5941), 756–760. https://doi.org/10.1126/science.1171958. ISSN 0036-8075, 1095-9203.

Larkum, Matthew E., Watanabe, Shigeo, Lasser-Ross, Nechama, Rhodes, Paul, Ross, William N., 2008. Dendritic properties of turtle pyramidal neurons. J. Neurophysiol. 99 (2), 683–694. https://doi.org/10.1152/jn.01076.2007.

Laurent, Gilles, 2020. On the value of model diversity in neuroscience. Nat. Rev. Neurosci. 21 (8), 395–396. https://doi.org/10.1038/s41583-020-0323-1.

Lauterbach, Marcel A., 2012. Finding, defining and breaking the diffraction barrier in microscopy – a historical perspective. Opt. Nanoscopy 1 (1), 8. https://doi.org/10.1186/2192-2853-1-8. ISSN 2192-2853. http://www.optnano.com/content/1/1/8.

Lauterbach, Marcel A., Keller, Jan, Schönle, Andreas, Kamin, Dirk, Westphal, Volker, Rizzoli, Silvio O., Hell, Stefan W., 2010. Comparing video-rate STED nanoscopy and confocal microscopy of living neurons. J. Biophoton. 3 (7), 417–424. https://doi.org/10.1002/jbio.201000038.

Lauterbach, Marcel Andreas, Guillon, Marc, Desnos, Claire, Khamsing, Dany, Jaffal, Zahra, Darchen, FranÃ.§ois, Emiliani, Valentina, 2016. Superresolving dendritic spine morphology with STED microscopy under holographic photostimulation. Neurophotonics 3 (4), 041806. https://doi.org/10.1117/1.NPh.3.4.041806.

Lee, Kea Joo, Kim, Hyun, Kim, Tae Sik, Park, Sun-Hwa, Rhyu, Im. Joo, 2004. Morphological analysis of spine shapes of Purkinje cell dendrites in the rat cerebellum using high-voltage electron microscopy. Neurosci. Lett. 359 (1–2), 21–24. https://doi.org/10.1016/j.neulet.2004.01.071. ISSN 03043940. https://linkinghub.elsevier.com/retrieve/pii/S0304394004001417.

Lee, Kea Joo, Kim, Hyun, Rhyu, Im. Joo, 2005. The roles of dendritic spine shapes in Purkinje cells. Cerebellum 4 (2), 97–104. https://doi.org/10.1080/14734220510007842. ISSN 1473-4222.

Luengo-Sanchez, Sergio, Fernaud-Espinosa, Isabel, Bielza, Concha, Benavides-Piccione, Ruth, Larrañaga, Pedro, DeFelipe, Javier, 2018. 3D morphology-based clustering and simulation of human pyramidal cell dendritic spines. PLOS Comput. Biol. 14 (6), e1006221 https://doi.org/10.1371/journal.pcbi.1006221. ISSN 1553-7358. https://dx.plos.org/10.1371/journal.pcbi.1006221.

Matsuzaki, Masanori, Honkura, Naoki, Ellis-Davies, Graham C.R., Kasai, Haruo, 2004. Structural basis of long-term potentiation in single dendritic spines. Nature 429 (6993), 761–766. https://doi.org/10.1038/nature02617. ISSN 1476-4687.

Motta, Alessandro, Berning, Manuel, Boergens, Kevin M., Staffler, Benedikt, Beining, Marcel, Loomba, Sahil, Hennig, Philipp, Wissler, Heiko, Helmstaedter, Moritz, 2019. Dense connectomic reconstruction in layer 4 of the somatosensory cortex. Science 366 (6469), eaay3134. https://doi.org/10.1126/science.aay3134.

Nusser, Zoltan, Naylor, David, Mody, Istvan, 2001. Synapse-specific contribution of the variation of transmitter concentration to the decay of inhibitory postsynaptic currents. Biophys. J. 80 (3), 1251–1261. https://doi.org/10.1016/S0006-3495(01)76101-2. ISSN 0006-3495.

Otor, Yara, Achvat, Shay, Cermak, Nathan, Benisty, Hadas, Abboud, Maisan, Barak, Omri, Schiller, Yitzhak, Poleg-Polsky, Alon, Schiller, Jackie, 2022. Dynamic compartmental computations in tuft dendrites of layer 5 neurons during motor behavior. Science 376 (6590), 267–275. https://doi.org/10.1126/science.abn1421.

Padmanabhan, Pranesh, Kneynsberg, Andrew, Götz, J.ürgen, 2021. Super-resolution microscopy: a closer look at synaptic dysfunction in Alzheimer disease. Nat. Rev. Neurosci. 22 (12), 723–740. https://doi.org/10.1038/s41583-021-00531-y.

Pchitskaya, Ekaterina, Bezprozvanny, Ilya, 2020. Dendritic spines shape analysis – classification or clusterization? perspective. Front. Synaptic Neurosci. 12, 31 https://doi.org/10.3389/fnsyn.2020.00031. ISSN 1663-3563. https://www.frontiersin.org/article/10.3389/fnsyn.2020.00031/full.

Peters, Alan, Kaiserman-Abramof, Ita R., 1970. The small pyramidal neuron of the rat cerebral cortex. The perikaryon, dendrites and spines. Am. J. Anat. 127 (4), 321–355. https://doi.org/10.1002/aja.1001270402. ISSN 0002-9106, 1553-0795.

Preibisch, Stephan, Saalfeld, Stephan, Tomancak, Pavel, 2009. Globally optimal stitching of tiled 3D microscopic image acquisitions. Bioinformatics 25 (11), 1463–1465. https://doi.org/10.1093/bioinformatics/btp184. ISSN 1367-4803.

Rangaraju, Vidhya, Lauterbach, Marcel A., Schuman, Erin M., 2019. Spatially stable mitochondrial compartments fuel local translation during plasticity. Cell 176 (1), 73–84. https://doi.org/10.1016/j.cell.2018.12.013. ISSN 0092-8674.

Riquelme, Juan Luis, Hemberger, Mike, Laurent, Gilles, Gjorgjieva, Julijana, 2023. Single spikes drive sequential propagation and routing of activity in a cortical network. eLife 12, e79928. https://doi.org/10.7554/eLife.79928. ISSN 2050-084X.

Runge, Karen, Cardoso, Carlos, de Chevigny, Antoine, 2020. Dendritic spine plasticity: Function and mechanisms. Front. Synaptic Neurosci. 12 https://doi.org/10.3389/fnsyn.2020.00036. ISSN 1663-3563.

Schikorski, T., Stevens, C.F., 1999. Quantitative fine-structural analysis of olfactory cortical synapses. Proc. Natl. Acad. Sci. USA 96 (7), 4107–4112. https://doi.org/10.1073/pnas.96.7.4107. ISSN 0027-8424, 1091-6490.

Sorra, K.E., Harris, K.M., 1993. Occurrence and three-dimensional structure of multiple synapses between individual radiatum axons and their target pyramidal cells in hippocampal area CA1. J. Neurosci. 13 (9), 3736–3748. ISSN 0270-6474.

Spacek, Josef, Harris, Kristen M., 2004. Trans-endocytosis via spinules in adult rat hippocampus. J. Neurosci. 24 (17), 4233–4241. https://doi.org/10.1523/JNEUROSCI.0287-04.2004. ISSN 0270-6474, 1529-2401.

Steffens, Heinz, Mott, Alexander C., Li, Siyuan, Wegner, Waja, Švehla, Pavel, Kan, Vanessa W.Y., Wolf, Fred, Liebscher, Sabine, Willig, Katrin I., 2021. Stable but not rigid: Chronic in vivo STED nanoscopy reveals extensive remodeling of spines, indicating multiple drivers of plasticity. Sci. Adv. 7 (24), eabf2806 https://doi.org/10.1126/sciadv.abf2806. ISSN 2375-2548.

Svara, Fabian, Förster, Dominique, Kubo, Fumi, Januszewski, Micha, dal Maschio, Marco, Schubert, Philipp J., Kornfeld, J.örgen, Wanner, Adrian A., Laurell, Eva, Denk, Winfried, Baier, Herwig, 2022. Automated synapse-level

reconstruction of neural circuits in the larval zebrafish brain. Nat. Methods 19 (11), 1357–1366. https://doi.org/10.1038/s41592-022-01621-0.

Tamada, Hiromi, Blanc, Jerome, Korogod, Natalya, Petersen, Carl C.H., Knott, Graham W., 2020. Ultrastructural comparison of dendritic spine morphology preserved with cryo and chemical fixation. eLife 9. https://doi.org/10.7554/elife.56384.

Tønnesen, Jan, Nägerl, U.Valentin, 2016. Dendritic spines as tunable regulators of synaptic signals. Front. Psychiatry 7, 101. https://doi.org/10.3389/fpsyt.2016.00101. ISSN 1664-0640.

Tønnesen, Jan, Katona, Gergely, Rózsa, Balázs, Nägerl, U.Valentin, 2014. Spine neck plasticity regulates compartmentalization of synapses. Nat. Neurosci. 17 (5), 678–685. https://doi.org/10.1038/nn.3682. ISSN 1546-1726.

Trommald, M., Hulleberg, G., Andersen, P., 1996. Long-term potentiation is associated with new excitatory spine synapses on rat dentate granule cells. Learn. Mem. 3, 218–228. https://doi.org/10.1101/lm.3.2-3.218. ISSN 1072-0502.

Waxman, S.G., Waxman, M., Pappas, G.D., 1980. Coordinated micropinocytotic activity of adjacent neuronal membranes in mammalian central nervous system. Neurosci. Lett. 20 (2), 141–146. https://doi.org/10.1016/0304-3940(80)90136-6. ISSN 03043940.

Westphal, V., Rizzoli, S.O., Lauterbach, M.A., Kamin, D., Jahn, R., Hell, S.W., 2008. Video-rate far-field optical nanoscopy dissects synaptic vesicle movement. Science 320 (5873), 246–249. https://doi.org/10.1126/science.1154228.

Westrum, Lesnick E., Blackstad, Theodor W., 1962. An electron microscopic study of the stratum radiatum of the rat hippocampus (regio superior, CA 1) with particular emphasis on synaptology. J. Comp. Neurol. 119 (3), 281–309. https://doi.org/10.1002/cne.901190303. ISSN 0021-9967, 1096-9861.

Willig, K.I., Rizzoli, S.O., Westphal, V., Jahn, R., Hell, S.W., 2006. STED microscopy reveals that synaptotagmin remains clustered after synaptic vesicle exocytosis. Nature 440 (7086), 935–939. https://doi.org/10.1038/nature04592.

Wilson, C.J., Groves, P.M., Kitai, S.T., Linder, J.C., 1983. Three-dimensional structure of dendritic spines in the rat neostriatum. J. Neurosci. 3 (2), 383–398. https://doi.org/10.1523/JNEUROSCI.03-02-00383.1983.

Yuste, Rafael, 2013. Electrical compartmentalization in dendritic spines. Annu. Rev. Neurosci. 36 (1), 429–449. https://doi.org/10.1146/annurev-neuro-062111-150455. ISSN 0147-006X, 1545-4126.

Yuste, Rafael, Denk, Winfried, 1995. Dendritic spines as basic functional units of neuronal integration. Nature 375 (6533), 682–684. https://doi.org/10.1038/375682a0. ISSN 1476-4687. https://doi.org/10.1038/375682a0.

Yuste, Rafael, Majewska, Ania, Holthoff, Knut, 2000. From form to function: calcium compartmentalization in dendritic spines. Nat. Neurosci. 3 (7), 653–659. https://doi.org/10.1038/76609. ISSN 1546-1726.

Yuste, Raphael, 2010. Dendritic Spines. MIT Press, Cambridge (MA).

Zaccard, Colleen R., Shapiro, Lauren, Martin-de Saavedra, Maria D., Pratt, Christopher, Myczek, Kristoffer, Song, Amy, Forrest, Marc P., Penzes, Peter, 2020. Rapid 3D enhanced resolution microscopy reveals diversity in dendritic spinule dynamics, regulation, and function. Neuron 107 (3), 522–537. https://doi.org/10.1016/j.neuron.2020.04.025. ISSN 08966273. https://linkinghub.elsevier.com/retrieve/pii/S0896627320303172.